Journal of Materials Chemistry A

ROYAL SOCIETY OF CHEMISTRY

PAPER

View Article Online
View Journal | View Issue

Cite this: *J. Mater. Chem. A*, 2026, **14**, 2235

Cobalt promotion of the InO_x–TiO_2 heterojunction for dual photothermal reduction of CO_2

Rocío Sayago-Carro,[a] Esperanza Fernández-García,[a] Irene Barba-Nieto,[b] Uriel Caudillo-Flores,[c] Lu Ma,[d] José A. Rodriguez,[be] Marcos Fernández-García *[a] and Anna Kubacka *[a]

Received 15th September 2025
Accepted 18th November 2025

DOI: 10.1039/d5ta07547e

rsc.li/materials-a

A series of cobalt-promoted indium–titanium composite oxides was synthesized using a microemulsion method. Their functional properties were investigated for the photothermal reduction of carbon dioxide. In this series, the indium content varied between 2.5 and 20%, while the cobalt percentage was kept constant at 4% throughout the series. In all cases, carbon monoxide formation occurred selectively through the reverse water gas shift reaction. The sample with 2.5% In maximized the synergistic use of the two energy sources, while the sample with 10% In showed the highest catalytic activity under both thermal and dual photo-thermo conditions. A physicochemical characterization was performed for all samples. The use of microscopy and X-ray absorption spectroscopy demonstrated that sub-nanometric indium entities, in combination with atomically dispersed cobalt oxide entities, achieved a balance between high thermal activity and significant synergy between light and heat in a catalytic process. The system with 10% indium is thus able to improve the thermal catalytic process through the use of light, providing an intensification procedure for the classic process.

1. Introduction

Global warming has been closely linked to greenhouse gas emissions, particularly carbon dioxide (CO_2), which is the primary contributor due to its high concentration in the atmosphere. Although greenhouse emissions account for a high proportion of those driven by the functioning of our society, in the short and medium term, it is essential to control their contribution to the carbon dioxide concentration in the atmosphere. This control can be achieved through the optimization of several technologies, implementing CO_2 emission-control and capture processes, but also considering the development of emission-free technologies, as well as novel approaches that may use carbon dioxide as a reactant in chemical reactions.[1]

A significant challenge in the field of renewable and sustainable energy research is the development of processes that can convert carbon dioxide into valuable chemicals.[2] The use of renewable solar energy to convert carbon dioxide into value-added products is considered a promising strategy to mitigate the effects of this greenhouse gas.[3] In this context, converting carbon dioxide into fuels requires a technology that relies on photoactive materials capable of enabling this conversion. Through light absorption, these materials can separate photogenerated charge carriers and convert, on their surface, the reactants involved in the transformation of the carbon dioxide molecule by interacting with such carrier species.[4] In recent years, a new technology has emerged that utilizes dual energy sources in a cooperative manner, potentially providing a beneficial effect. Several energy sources can be used in catalysis, with light being one of the primary energy suppliers. Light has been coupled with conventional heat, electricity, magnetic fields, mechanical compression, stress, and others.[5,6] Known as photothermal catalysis, light and heat can be applied simultaneously to a chemical, catalytic reaction to drive various thermochemical and photochemical processes that synergistically enhance catalytic reactions.[7,8]

Photothermal catalysis can provide an energy-efficient and suitable route for the hydrogenation of carbon dioxide molecules, producing a multitude of industrially interesting products, such as carbon monoxide.[9] The hydrogenation of CO_2 primarily forms this molecule through the reverse water–gas shift reaction.[10,11] To carry out the photothermal valorization of CO_2, it is necessary to develop catalysts that efficiently utilize thermal and light inputs and simultaneously optimize selectivity towards a single product, such as CO in this case, thereby limiting waste and/or separation steps.[12] Nevertheless, creating such photothermal catalysts that are both cost-effective and

[a]*Instituto de Catálisis y Petroleoquímica, Consejo Superior de Investigaciones Científicas (ICP-CSIC), C/Marie Curie 2, 28049 Madrid, Spain. E-mail: mfg@icp.csic.es; ak@icp.csic.es*

[b]*Chemistry Division, Brookhaven National Laboratory, Upton, New York 11973, USA*

[c]*Centro de Nanociencias y Nanotecnología, Universidad Nacional Autónoma de México, Ensenada 22800, Mexico*

[d]*National Synchrotron Light Source II, Brookhaven National Laboratory, Upton 11973, NY, USA*

[e]*Department of Chemistry, Stony Brook University, Stony Brook, NY, 11794, USA*

highly efficient remains a significant challenge.[13] Still, the benefits would be multiple. On the one hand, achieving synergy between the two energy sources aims to limit the harsh operational conditions of CO_2 conversion thermal processes, which can lead to deactivation and reduced stability during prolonged operation. It also aims to increase the use of photons in photocatalysis and improve the quantum efficiency of the reaction. In summary, a fruitful combination of light and heat should lead to high activity and selectivity, as well as stability under long-term operational conditions.[12]

To reach such an ambitious objective, multicomponent composite materials are frequently utilized in catalysts. They can combine adequate thermal and photo capabilities with the appropriate surface chemistry for the reaction.[7,8] A major contributor in this context is composite materials, which have titania oxide as their main component, the most widely used photocatalyst. Titania is often combined with oxides that can be particularly efficient in interacting with carbon dioxide due to their basicity, such as indium oxide. The effects of the nanostructure and interface in these binary-oxide systems have been heavily investigated, and it is now essentially an open field.[14,15]

In this work, we have developed materials based on indium oxide sub- and nanostructures in contact with the pure anatase polymorph of titanium oxide, through atomically dispersed cobalt-containing species, for the energy- and chemically efficient photothermal valorization of the CO_2 molecule. Both indium oxide and titanium oxide possess nanostructures and defects that control the catalytic properties of these semiconductors, resulting in the promotion of CO_2 valorization activity under combined heat-light excitation.[16–18] It will be shown that cobalt bridging promotes the functional properties of these two solids. A detailed physicochemical characterization of the resulting composite materials is presented here to identify the most successful structures of the composite system. The intimate contact between the components is thus explored through a multitechnique approach using various tools such as high-resolution transmission electron microscopy (HR-TEM), X-ray absorption spectroscopy (XAS), and others. The manuscript utilizes XAS to provide a clear view of the local active structure of the materials and interpret the functional properties of the catalysts. To this end, the study not only investigates such local structures in the initial materials but also after prolonged use of those catalysts that show high and stable activity.

2 Materials and methods

2.1 Synthesis and characterization

2.1.1 Synthesis. The synthesis of all the catalysts in the series was carried out using the reverse microemulsion method. First, two organic phase solutions were prepared, composed of *n*-heptane, Triton X-100 as a surfactant, and hexanol as a co-surfactant, with the same content in both (water-to-surfactant ratios of 18). These two solutions were stirred magnetically for 30 min. After this time, a different solution was added to each: to the first, a solution of indium nitrate and water, and to the second, a solution of tetramethylammonium hydroxide (TMH; Aldrich) and water. Once these were added, the two main solutions were stirred for 1 h. After that, the TMH solution was added to the indium nitrate solution to precipitate indium oxide, resulting in a single solution. Half an hour later, a solution of cobalt and water was added. After stirring for 5 min, the titania precursors were added. This final solution was kept under magnetic stirring overnight. The next day, it was centrifuged and dried in an oven at 110 °C for 12 h, yielding an amorphous solid. Finally, to obtain the desired oxide phase, the material was calcined at 500 °C for 2 hours. The samples were named *x*In–4Co–Ti where *x* is the molar content of In with respect to Ti. This parameter varied between 2.5 to 20%. The cobalt content is fixed at 4 mol% as discussed in Section 3.

2.1.2 Characterization. A comprehensive characterization of the synthesized catalysts was conducted using a variety of physicochemical techniques. Initial analysis focused on the basic properties of the materials. Elemental analysis of the samples was performed using inductively coupled plasma atomic emission spectroscopy (ICP-OES) (PerkinElmer Optima 3300 DV). Specific surface area and porosity were studied using nitrogen adsorption–desorption isotherms (BET method) after the catalysts were degassed overnight at 140 °C, utilizing a Micromeritics Tristar-II 3020 apparatus (USA). The crystalline structure of the samples was examined using X-ray diffraction (XRD), performed on a Bruker D8 Advance diffractometer with Ni-filtered Cu-Kα radiation ($\lambda = 0.15406$ Å). Optical properties, specifically the bandgap, were analyzed using UV-vis diffuse reflectance spectroscopy with a Varian Cary 300 spectrophotometer (USA), with a Teflon film serving as the reference.

To gain deeper insights into the structure of the catalysts, both at the long-range and local level, advanced techniques were also employed. Photoluminescence (PL) spectroscopy was carried out using a Horiba FluoroMax Plus spectrofluorometer (Germany), with excitation at 365 nm. Morphological features and particle sizes were investigated by scanning transmission electron microscopy (TEM). STEM analysis was performed in high-angle annular dark-field (HAADF) mode in a Cs-corrected JEOL ARM200F microscope (LUME@UNAM, RRID: SCR_024400). The equipment is equipped with an Oxford AZtecTEM silicon detector for energy-dispersive X-ray spectroscopy (EDS). Around 50 images per sample were used to assess particle size distribution and morphology.

X-ray photoelectron spectroscopy (XPS) was conducted using a SPECS® system (UK), equipped with a PHOIBOS® 150 WAL hemispherical analyzer, an XR 50 Al-X-ray source, and a μ-FOCUS 500 monochromator. Binding energy corrections for surface charging were done by referencing to the C 1s signal at 284.6 eV. Spectral deconvolution was performed using CASA software (version 2.3.25), with a Shirley background correction applied.

Surface acidity and adsorption behavior were evaluated using temperature-programmed desorption (TPD). Experiments were conducted in a custom-built U-shaped reactor coupled with a thermal conductivity detector (TCD). Samples were first saturated with CO_2 at 50 °C, purged with nitrogen until a stable baseline was achieved (approx. 30 minutes), and then subjected to a heating ramp of 10 °C min^{-1}.

Finally, X-ray absorption spectroscopy (XAS) measurements at the K-edges of cobalt (7709 eV) and indium (27 940 eV) were carried out in fluorescence mode at the 8-ID and 7-BM beamlines, respectively, of the National Synchrotron Light Source II (NSLS-II) at Brookhaven National Laboratory. Powder samples were dispersed onto Kapton tape for the measurements. Energy calibration was performed using Co or In foil, which was measured simultaneously with the samples. At the 8-ID beamline, the X-ray optics include a collimating mirror system with a Pt/Si/Rh coating, a high heat load Si(111) monochromator, a focusing toroidal mirror with Pt/Rh coating, and a high harmonic rejection mirror system (Rh/Si/Pt) situated in the end-station.[19] Additional focusing is achieved through a polycarpellary lens installed at the end-station. At the 7-BM beamline, the optics consist of a Rh-coated collimating mirror, a Si(111) double-crystal monochromator, a Rh-coated harmonic rejection mirror, and a polycapillary lens for beam focusing at the sample position. The phase and amplitude functions were derived from the CoO (space group $Fm\bar{3}m$) and Co-doped In_2O_3 (Bixbite-type with space group $Ia\bar{3}$) structures.

2.2 Catalytic activity measurements

The activity measurements for the photothermal valorization of CO_2 using the developed series of catalysts were carried out in a continuous-mode cylindrical Pyrex glass reactor, where the material was distributed as a homogeneous film. Coaxially surrounding this first cylinder is another, made of the same material, allowing gas flow between them and in contact with the catalytic film. The thinness of the film enables uniform interaction with both temperature and light at all points. Inside the reactor, a regulated resistance serves as the thermal source. This entire system is housed within a chamber equipped with four lamps, symmetrically arranged around the reactor, to provide illumination. The reaction mixture, consisting of CO_2, H_2, and N_2 at a total flow rate of 10 mL min^{-1}, was prepared with a CO_2 : H_2 ratio of 1 : 1. An Agilent GC 8890B was connected online to the reactor outlet and used to monitor the reaction gases, employing two thermal conductivity detectors (TCDs) and one flame ionization detector (FID). This setup enabled the evaluation of both the activity and selectivity of the reaction. The reaction was evaluated across a temperature range from room temperature to 350 °C, both under dark conditions and with illumination at each temperature. Comprehensive details of the experimental setup, energy sources, gas handling system, reaction environment, detection methods for reactants and products, and reaction protocols are summarized in the SI section.

3. Results and discussion

3.1 Synthesis and general physico-chemical characterization of composites

The solids were synthesized using a single-pot procedure (schematized in Fig. 1) *via* a reverse microemulsion method, which allows for the fine control of the nanostructural properties, as well as the contact between the components of the composite materials.[20] Our goal was to finely disperse the cobalt and indium-containing species onto the titania surface. With this aim, we first synthesized the indium solid precursor by precipitating the corresponding cation with TMH in the microemulsion droplets (initial step in Fig. 1). Once this is done, cobalt cations were added to the solution (second step in Fig. 1) and maintained in agitation until the titania precursor was introduced. Being a Ti alcoxy-type precursor, it is hydrolyzed in the presence of water molecules enclosed in the reverse microemulsion droplets, simultaneously drawing the cobalt ions. After calcination (Fig. 1), ICP-OES indicates that the In and Co contents of all materials correspond to the In/Ti and Co/Ti synthesis ratios within an error of 4.8%. In the series under study, a Co content of *ca.* 4% was fixed for all samples, as it corresponds to a content that maximizes the functional properties for the cases of single-oxide indium and titanium.[21–23] The indium content was explored up to a content of *ca.* 20%. As detailed below, this is the limit at which nano-type behavior can be obtained for this component. As shown in Fig. 1 for selected examples, the materials show nitrogen adsorption–desorption isotherm profiles typical of microporous materials. For all samples, the isotherms display a characteristic H4-type loop dominated by adsorbate–solid interactions.[24] As summarized in Table 1, all catalysts are high surface area mesoporous materials. They exhibit BET surface areas between *ca.* 85 and 100 m^2 g^{-1}.

TEM analyses were performed to further characterize the morphology and structure of the materials. The TEM micrographs for the 2.5In–Co–Ti and 10In–Co–Ti samples are presented in Fig. 2, panels A–B and C–D, respectively. As shown in the corresponding EDS analyses (Fig. 2E–N), well-dispersed entities of both indium and cobalt are clearly visible, confirming the dispersion of both species over the major-component titanium as well as the proximity at the nano-scale between the cobalt and indium entities. The digital diffraction patterns obtained from the TEM micrographs show that the major component displays the anatase structure (Fig. 2A and C). This is confirmed by the XRD characterization results. Such results are shown in Fig. 2O. First, note that the pattern dominating the XRD signal, corresponding to the titania component, visible in all samples, corresponds to the mentioned anatase polymorph (JCPDS card 21-1272; $I4_1/amd$ space group).[25] Also, peaks corresponding to the bixbyite structure of cubic body-centered In_2O_3 (bcc) would be visible.[26] The most intense peak, assigned to the (222) reflection (as can be observed in the pure In_2O_3 reference; Fig. 2O), appears as a broad feature for the 15In–Co–Ti sample, and as a well-developed peak for the 20In–Co–Ti catalyst. It can be noted that the anatase pattern is thus maintained throughout the series, with the absence of peaks associated with indium oxide for samples with an indium content below 15% or associated with cobalt-containing phases for all solids. Similar to the XRD patterns, the UV-vis spectra display strong similarities between samples. They are shown in Fig. 2P. The reference In_2O_3 oxide exhibits strong absorption in the UV region (<400 nm), with an abrupt drop, which is typical of a semiconductor with a relatively wide band gap. The reference titanium oxide (pure anatase) also shows strong

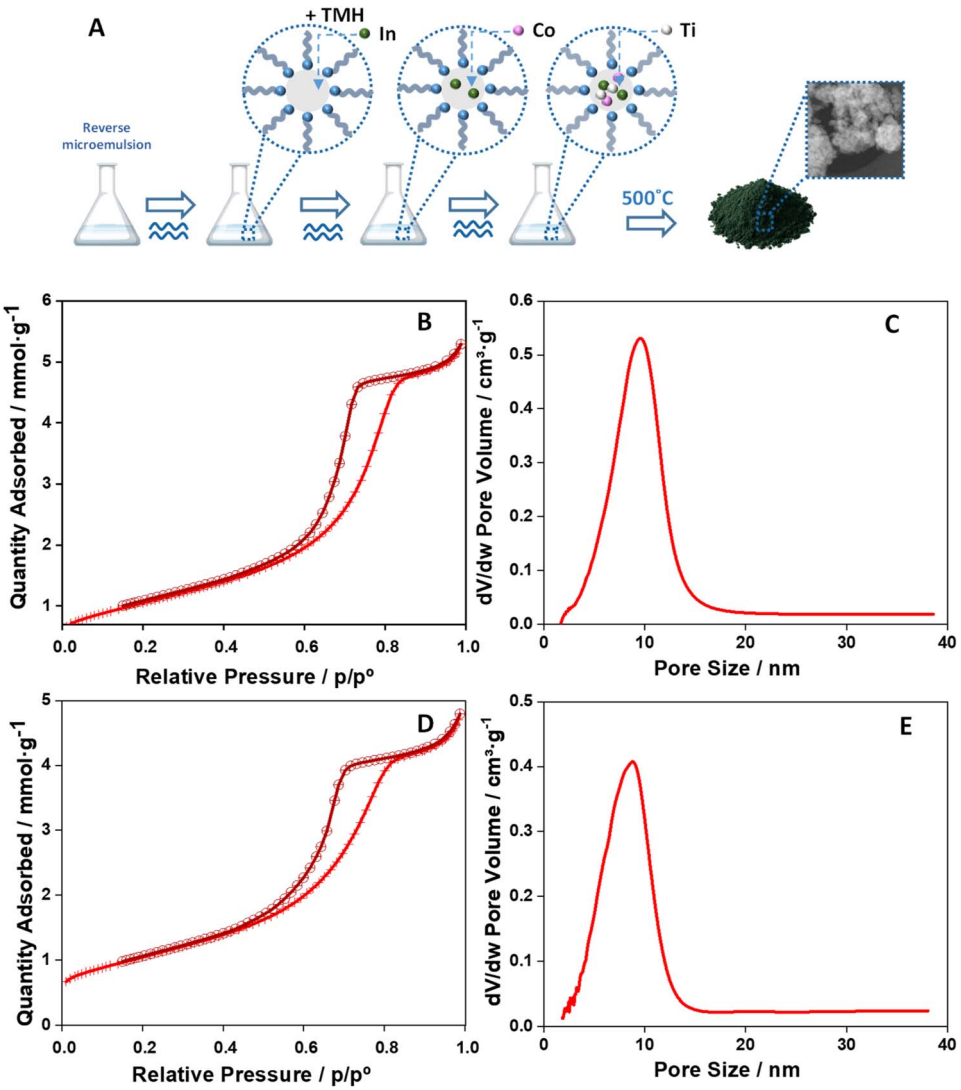

Fig. 1 (A) Schematic representation of the synthesis carried out using the reverse microemulsion method. (B) Nitrogen adsorption–desorption isotherm results for the 2.5In–Co–Ti sample. (C) Pore volume distribution for the 2.5In–Co–Ti sample. (D) Nitrogen adsorption–desorption isotherm results for the 10In–Co–Ti sample. (E) Pore volume distribution for the 10In–Co–Ti sample.

absorption in the UV region, starting to absorb at slightly shorter wavelengths than In_2O_3.[27] For all catalysts, it can be observed that as the In content increases, there is a redshift of the absorption edge, possibly indicating a decrease in the band gap energy.[28] However, the UV-visible spectra are dominated by the major anatase components in all composite solids.

Table 1 BET area, pore volume and anatase primary particle size of the samples[a]

Sample	BET area ($m^2\ g^{-1}$)	Pore volume ($cm^3\ g^{-1}$)	Anatase particle size (nm)
T	146	0.17	8.8
I	146	0.46	6.2
2.5In–Co–Ti	88	0.17	12.5
5In–Co–Ti	96	0.19	12.1
10In–Co–Ti	85	0.19	13.8
15In–Co–Ti	100	0.18	12.3
20In–Co–Ti	90	0.18	14.8

[a] Average standard error: BET area 9.7%; pore volume 8.6%, anatase particle size 6.4%.

3.2 Structural and electronic analysis of In and Co components

The initial stage (pre-reaction) characterization, focusing on the minor components, was carried out using a multitechnique procedure. As a first technique, the catalysts were further examined through the XPS analysis of the powders. Fig. 3A presents the Co 2p XPS spectra for all samples in their initial state. The Co $2p_{3/2}$ signal peaks at *ca.* 780.0–780.1 eV in all cases. This binding energy highlights the existence of Co(II) type species.[29] To gain a deeper understanding of the oxidation state of the cobalt species and their location within the composite, the materials were studied using XAS. The results of the XANES (X-ray near-edge spectroscopy) analysis corresponding to the Co

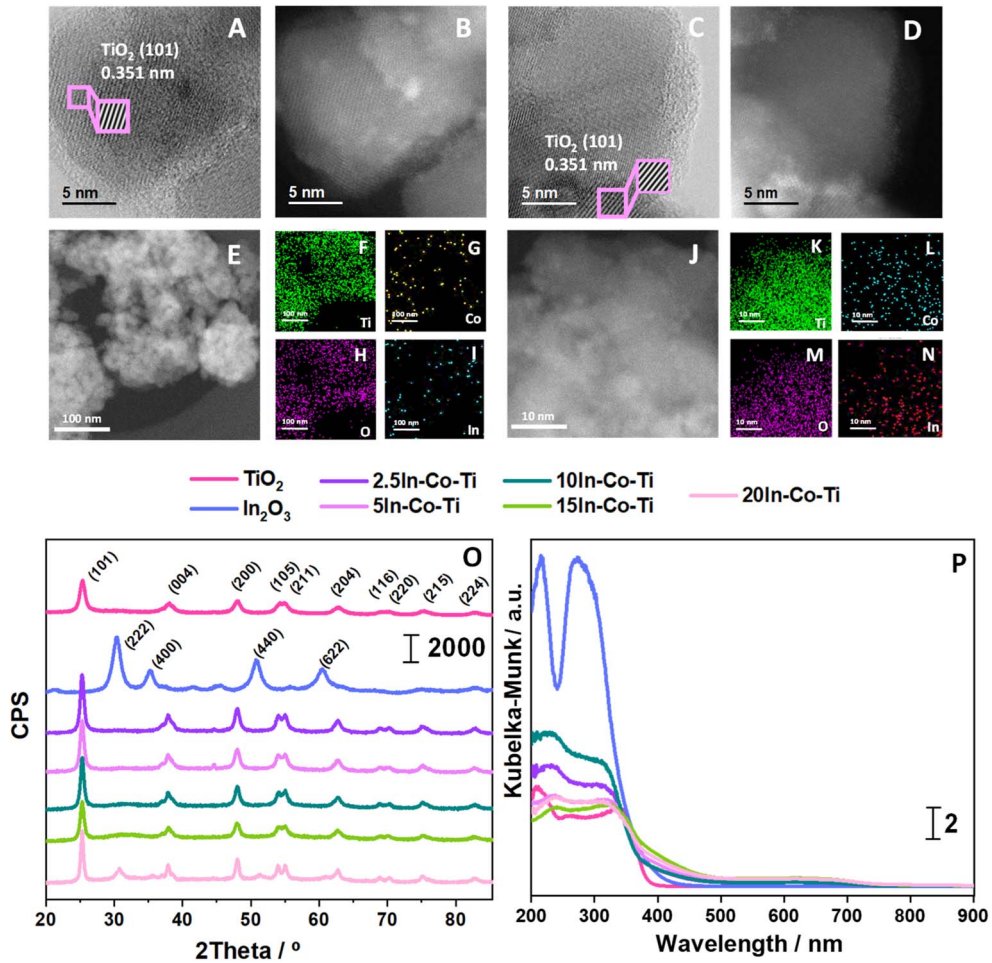

Fig. 2 (A and B) TEM micrographs for the 2.5In–Co–Ti sample. (C and D) TEM micrographs for the 10In–Co–Ti sample. (E–I) Dark-field STEM (E) and EDS mapping for the 2.5In–Co–Ti sample. (J–N) Dark-field STEM (J) and EDS mapping for the 10In–Co–Ti sample. (O) XRD patterns for the *x*In–Co–Ti and reference samples. (P) UV-visible plot spectra for the *x*In–Co–Ti samples.

K-edge can be seen in Fig. 3B. The use of XAS with respect to XPS has advantages, particularly in the case of sub-nanometric cobalt-containing species. All samples of the system have been analyzed, as well as the corresponding references corresponding to CoO, Co_2O_3 oxides, and metallic Co. The higher intensity of the white line (exemplified by the intensity value at *ca.* 7724 eV) with respect to the CoO and Co_2O_3 oxide references points out the increased degree of the covalent character of the Co(3d)–O(2p) interaction in the initial state of the samples with respect to the mentioned references. This fact is characteristic of sub-nanometric and/or isolated Co(II) type species.[30] To provide more detail about the cobalt oxidation state, the widely applied integral method was employed.[31] In this way, it was shown that the catalyst 2.5In–Co–Ti has an intermediate oxidation state of 2.57 and that the sample 10In–Co–Ti has an oxidation state of 2.24. Therefore, the significant differences in the white line with respect to the reference systems can be attributed to the limited size of the cobalt entities, which exhibited average oxidation states above two but below three due to their specific local environments. This shows that the cobalt-containing entities are strongly defective in terms of both the structure (sub-nanometric) and electronic structure. TEM images of the 2.5In–Co–Ti and 10In–Co–Ti samples are presented in Fig. 3C and 2D, respectively. In the analysis of these images, planes with a distance of 0.352 nm have been identified, which corresponds to the (101) plane of titania in its anatase form.[32] In addition, cobalt entities can be observed, with planes with a distance of approximately 0.229 nm, roughly corresponding to the (102) plane of Co_2O_3 (JCPDS card 02-0770), which would confirm that the local Co(II) and Co(III) type environments would co-exist. This will be further investigated using EXAFS.

The study of the indium-containing entities was also conducted. At a first glance at the In $3p_{3/2}$ XPS peak (Fig. 3E), it is observed that its maximum is located at a binding energy of 665.0 eV, remaining unchanged throughout the series of catalysts. This binding energy corresponds to an In(III) oxidation state.[33] This point is corroborated using the XANES fingerprints present in the corresponding In K-edge spectra (Fig. 3F). For all samples, such XANES spectra exhibit an invariant absorption edge energy of *ca.* 27 938.0 eV. This is the same binding energy that was obtained in the pure indium oxide in ref. 34. Moreover,

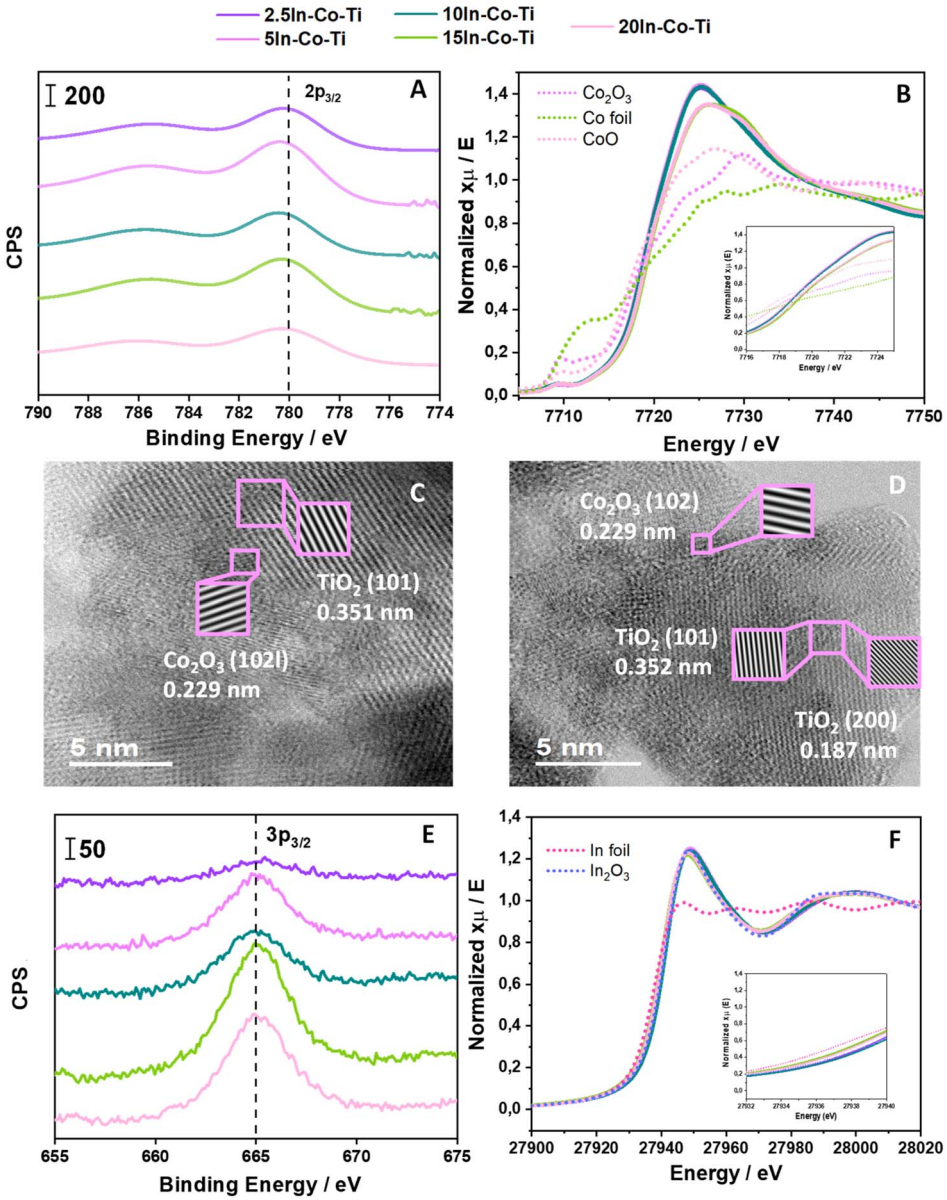

Fig. 3 (A) Co $2p_{3/2}$ XPS spectra for the *x*In–Co–Ti samples. (B) Co K-edge XANES spectra for the *x*In–Co–Ti catalysts and reference samples. (C) TEM micrographs for the 2.5In–Co–Ti sample. (D) TEM micrographs for the 10In–Co–Ti sample. (E) In $3p_{3/2}$ XPS spectra for the *x*In–Co–Ti samples. (F) In K-edge XANES spectra for the *x*In–Co–Ti catalysts and reference samples.

variations in the white line intensity are relatively minor compared to the mentioned In_2O_3 reference. Thus, the In(III) oxidation state can be confirmed for all samples.

As mentioned, EXAFS was used to further analyze the local environment of the minor components, cobalt and indium. The local environment of Co is analyzed in more detail in Fig. 4A. The Fourier transform magnitudes of the signals for all catalysts in the series, as well as for the reference systems used, are depicted in this figure. Two peaks are clearly visible in the Fourier transform signals. The first peak, ascribable to the Co–O shell, shows close resemblance with the Co_2O_3 reference, indicating a coordination number close to a 6-fold coordination. Substantial differences are observed with respect to the references for higher shells. To further progress, we fitted the experimental signals. According to the Nyquist theorem,[35,36] the *k* and *R*-ranges available for EXAFS fitting (see Table 2) allow for a number of free parameters exceeding 12 in all cases. So, a three-shell fitting was attempted for all cases. The results of the fitting are summarized in Table 2. The comparison between the fitting results and experimental signals (module and real part of the Fourier transform) is visualized in Fig. 4B–D. Two cation–cation shells corresponding to Co–Co and Co–Ti contributions were observed for all samples. The fitting results for these two shells allow for inferring the local order around the cobalt atoms. The coordination numbers and distances for these two shells are presented in Fig. 4E and F. Considering the

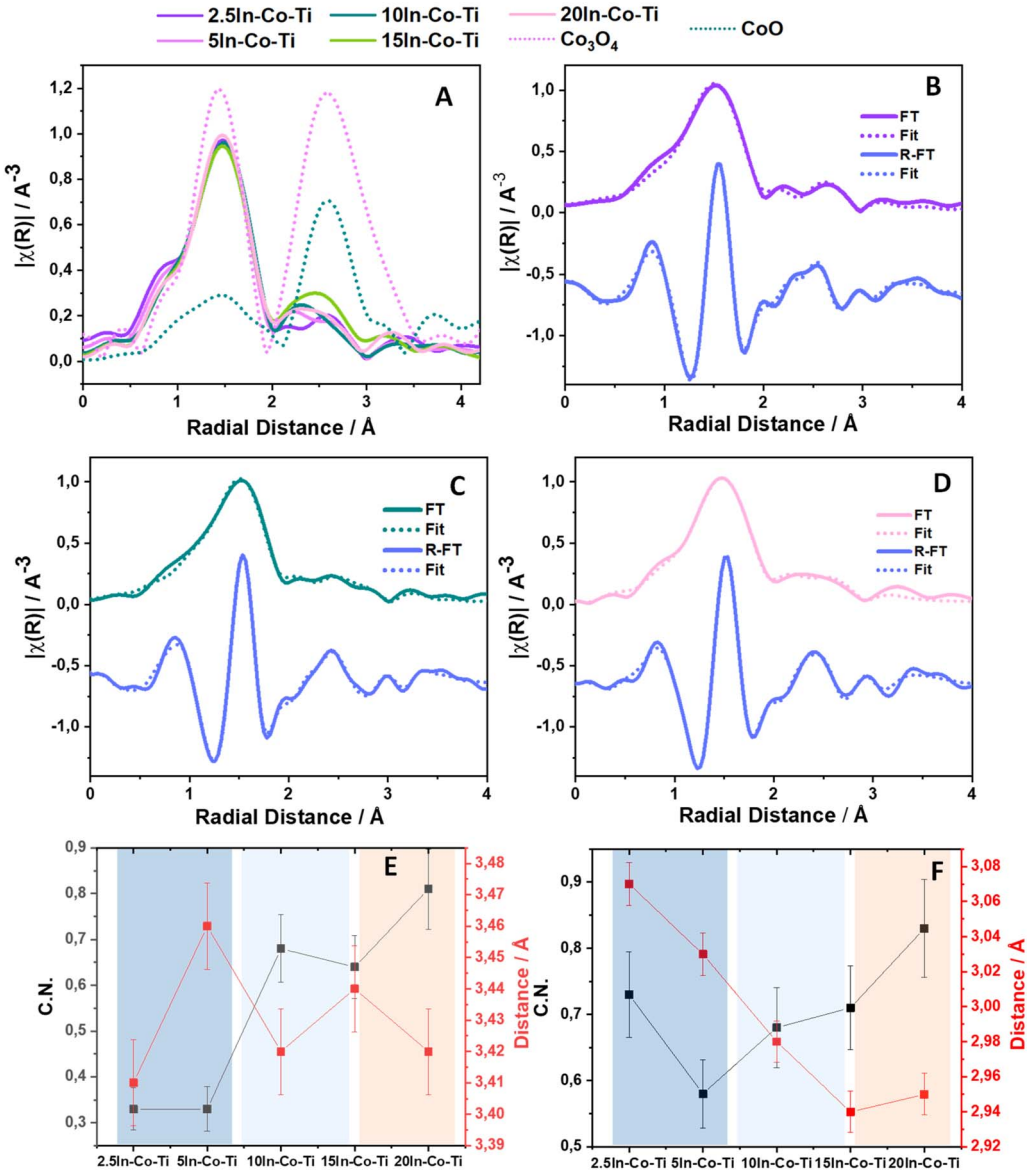

Fig. 4 (A) K^2-weighted Fourier Transform (FT) of the Co K-edge EXAFS signal for the catalysts and reference samples. (B–D) Real part (R-FT) and module (FT) of the Fourier transform for selected samples. Experimental signals (R-FT and FT) and fitting results are presented. (E) Coordination number (C. N.) and distance of the Co–Co shell for the *x*In–Co–Ti samples. (F) Coordination number (C. N.) and distance of the Co–Ti shell for the *x*In–Co–Ti samples.

Co–Co shell, the coordination distance is roughly constant and typical of the oxidic environments. However, the coordination numbers are always below 1, indicating the relatively small size of the cobalt-containing entities. An important increase (out of experimental error) in the coordination number is observed for the 10In–Co–Ti sample and those with higher indium content. For the Co–Ti shell, the (Co–Ti) coordination number is also below 1. The distance varies significantly between the samples, up to the 15In–Co–Ti catalyst. This distance varies in an important range (from 3.07 to 2.96 Å) and does not match the Ti–O–Ti distances of anatase (which are around *ca.* 3.0 Å).[25] The smallest size of Co would result in a distance below the mentioned 3.0 Å.[37] The variability in the coordination distance, as well as the presence of Co–Co distances typical of cobalt oxides in the anatase lattice (as detected with TEM, Fig. 3C and D), suggests that a substitutional doping of the anatase oxide is unlikely to occur. Taking all these facts into account, we can note that the cobalt-containing clusters are at the surface of the major anatase component. They are relatively small for samples below 10In–Co–Ti and then start to grow (see the Co–Co coordination number; Fig. 4E) for this sample and samples with higher indium content. The 20In–Co–Ti sample appears different both in terms of the Co–Co and Co–Ti contributions. Based on the coordination numbers and distances observed, we can infer that samples below 10In–Co–Ti contain nearly isolated cobalt-containing entities. Above this sample, these clusters

Table 2 Co K-edge EXAFS fitting results for the samples. Catalyst names are followed by *k* and *R* ranges used for fitting[a]

Shell	*N*	*R*/Å	$\Delta\sigma^2/10^3$ Å^2	E_0/eV
2.5In–Co–Ti; *k*: 2.55–10.06 Å^{-1}; *R*: 1.01–3.42 Å				
Co–O	4.7	2.00	8.5	−4.8
Co–Ti	0.7	3.07	9.0	−4.8
Co–Co	0.3	3.41	6.5	−4.8
5In–Co–Ti; *k*: 2.54–10.46 Å^{-1}; *R*: 1.01–3.43 Å				
Co–O	5.0	1.99	8.0	−4.8
Co–Ti	0.6	3.03	9.0	−4.8
Co–Co	0.3	3.46	4.7	−4.8
10In–Co–Ti; *k*: 2.55–10.98 Å^{-1}; *R*: 1.01–3.44 Å				
Co–O	5.1	1.99	8.0	−3.8
Co–Ti	0.7	2.98	9.0	−3.8
Co–Co	0.7	3.42	7.0	−3.8
15In–Co–Ti; *k*: 2.55–10.97 Å^{-1}; *R*: 1.01–3.42 Å				
Co–O	4.8	1.99	9.1	−4.4
Co–Ti	0.5	2.94	8.4	−4.4
Co–Co	0.6	3.44	9.0	−4.4
20In–Co–Ti; *k*: 2.55–11.37 Å^{-1}; *R*: 1.01–3.42 Å				
Co–O	5.8	1.98	8.0	−4.8
Co–Ti	0.4	2.95	8.0	−4.8
Co–Co	0.8	3.42	7.0	−4.8
2.5In–Co–Ti–T; *k*: 2.55–10.01 Å^{-1}; *R*: 1.01–3.42 Å				
Co–O	4.7	2.01	8.5	−4.7
3.Co–Ti	0.7	3.07	9.0	−4.7
Co–Co	0.4	3.41	6.5	−4.7
2.5In–Co–Ti–TP; *k*: 2.55–10.15 Å^{-1}; *R*: 1.01–3.43 Å				
Co–O	4.7	2.01	9.2	-4.7_5
Co–Ti	0.7	3.07	9.0	-4.7_5
Co–Co	0.4	3.42	6.5	-4.7_5
10In–Co–Ti–T: *k*: 2.53–10.89 Å^{-1}; *R*: 1.01–3.44 Å				
Co–O	5.1	2.00	8.0	−5.3
Co–Ti	0.6	3.05	9.0	−5.3
Co–Co	0.6	3.44	9.0	−5.3
10In–Co–Ti–TP: *k*: 2.55–11.06 Å^{-1}; *R*: 1.01–3.44 Å				
Co–O	5.1	2.00	9.2	−5.0
Co–Ti	0.6	3.05	9.0	−5.0
Co–Co	0.6	3.44	9.0	−5.0

[a] Average standard error: *N*; 10.3%, *R* 0.01 Å; Debye–Waller factor; 11.3%; *E* 1 eV.

start to grow, leading to the appearance of two-atom cobalt entities. Both entities interact strongly with the anatase surface. At a certain point (near or above the 15In–Co–Ti sample), the cobalt entities appear to be stabilized in terms of the Co–Ti interaction.

The EXAFS analysis of the indium species was also carried out. Fig. S2 displays the Fourier transform of the samples and the indium oxide reference. As can be seen in the figure, after the first In–O shell (the first peak of the Fourier transform), the samples exhibit significant differences with respect to the reference. All samples, except the 20In–Co–Ti samples, show strong similarities, with a relatively weak signal after the first In–O shell, indicating a limited growth in primary particle size. The signal is so weak that it cannot be fitted easily. The 20In–Ti–Co sample, however, displays a stronger signal in the 3–4 Å interval. This signal resembles the one displayed by the indium oxide reference, which includes In–In distances at *ca.* 3.4 and 3.8 Å,[26] but at shorter distances (Fig. S2). This suggests that up to *ca.* 15% loading, the indium species are somewhat similar in terms of their local environment, both at the electronic (XANES) and structural (EXAFS) levels. In the case of the 20In–Co–Ti sample, the mentioned (cation–cation shells) component seems to have a nano-structure with a certain resemblance to the indium oxide reference.

The combined Co and In K-edge EXAFS study would thus indicate that the different structural characteristics of the cobalt and indium entities define three different zones, as identified in Fig. 4E and F. The first two are identified by the presence of sub-nanometric species for the two cations, while the third contains nano-metric indium oxide-type entities.

3.3 Optical and photothermo catalytic properties

In Fig. 5, panels A and B, we display the optical properties relevant to interpreting activity for representative samples. According to eqn (S2) and (S3) (see the SI section), they should be used to calculate the quantum efficiency of the samples. The quantum efficiency is the parameter specified by the IUPAC to measure the activity of any photocatalytic process.[38] The fraction of the transmittance and reflection of the samples, together with the contribution attributable to thermal losses, is used to calculate the local surface rate of photon absorption at the reaction temperature (eqn (S3) in the SI). The plots of the optical properties show a region below *ca.* 400 nm with behavior reflecting the dominant effect of the band gap of the anatase component. Afterwards, the plots display a region dominated by the indium component. Fig. 5C and D display the local surface rate of photon absorption of the films used to carry out the reaction for the 2.5In–Co–Ti and 10In–Co–Ti samples. Significant differences are observed between the two samples, reflecting their distinct interactions with light at a reaction temperature of 250 °C. As shown in Fig. S3, this temperature is selected because it maximizes the promotion of the dual photothermal activity for both samples. We scanned the reaction from room temperature (when light alone is used, this corresponds to the "pure" photo result) up to 350 °C (Fig. S3). The synergy between the light and heat sources is calculated according to eqn (S1). Such an equation defines the so-called (reaction rate) excess function, a quantitative measure of the enhancement achieved for the joint use of the two energy sources. All samples display excess function values increasing up to 250 °C. After this point, they decrease and, near 350 °C, become moderately negative.

The values taken by the reaction rate, (reaction rate) excess function, and quantum efficiency parameters at the mentioned temperature (250 °C) are displayed in Fig. 5E for all samples under study. The single-source thermal reaction rates of the samples increase with indium content up to *ca.* 10%, and then

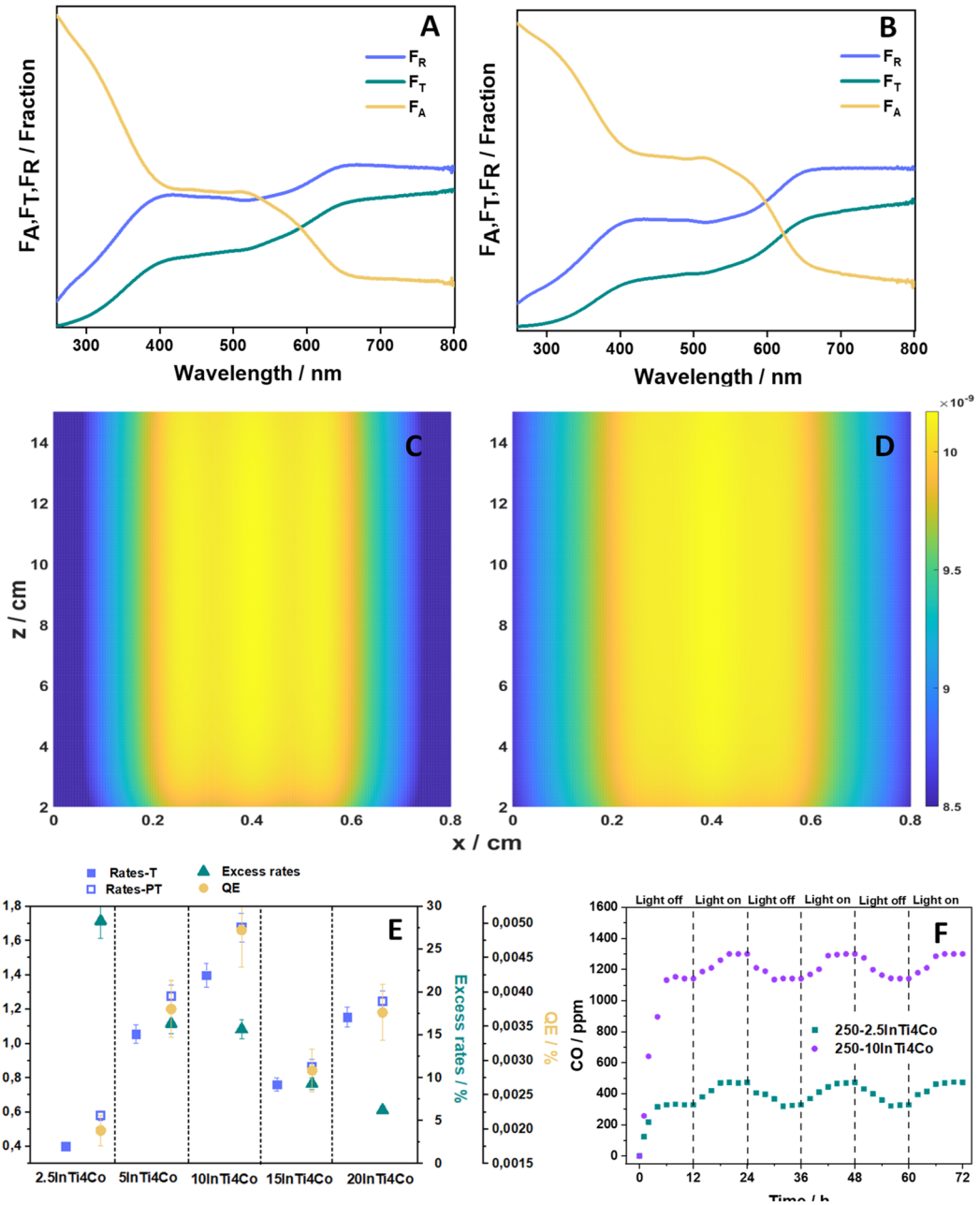

Fig. 5 (A and B) Fraction of light absorbed, transmitted or reflected by the 2.5In–Co–Ti and 10In–Co–Ti samples, respectively. (C and D) Local photon absorption rate at 250 °C (einstein m^{-2} s^{-1}) under irradiation for the 2.5In–Co–Ti and 10In–Co–Ti samples, respectively. (E) Reaction rates, excess rates and quantum efficiency for *x*In–Co–Ti samples. (F) Long-term operation tests for selected samples under light off/on cycling conditions.

decrease moderately afterwards. The behavior of the photothermal rate is entirely different. The excess parameter provides strong evidence of this behavior. It reaches the maximum value for the 2.5In–Co–Ti samples. Afterwards, it shows a stability region for samples up to the 10In–Co–Ti one, and then decreases for the 15 and 20-In–Co–Ti catalysts. Note that the efficiency in the use of photons, measured by the quantum efficiency parameter, reaches the maximum for the 10In–Co–Ti material. This parameter accounts for the different optical properties (including absorption, as described in eqn (S2)) of the samples and thus provides a measurement of the catalytic activity per absorbed photon. The joint analysis of the three parameters indicates that the single-source thermal and light contributions increase up to the sample containing *ca.* 10% In. Nevertheless, the positive effect of energy sources appears to decrease with the indium content of the materials.

To compare single and dual energy catalytic processes, it should be considered that the single-source thermal effect provides a reaction rate (at 250 °C) about two orders of magnitude higher than that of the single-source light-alone

counterpart (Fig. S3). Therefore, we can stress that we obtained a sample where thermal effects are limited, but the synergistic combination with light is maximum in the 2.5In–Co–Ti sample. Additionally, it is observed that the 10In–Co–Ti sample, which exhibits maximum catalytic activity under dual excitation, is characterized by a heat effect that is maximized and a moderate combined effect of the energy sources. The analysis of the activation energy of the reaction in the region of maximum excess (around 250 °C) points out the differences between catalysts (Fig. S4). The combined excitation with light shows a more significant effect for the 2.5In–Co–Ti catalyst (*ca.* 31 kJ mol^{-1} decrease) than the 10In–Co–Ti sample (*ca.* 18 kJ mol^{-1}). In addition, the comparison of thermal and photothermal experiments for these two samples points out the critical role played by cobalt in the reaction (Fig. S4), which is further examined below using infrared spectroscopy.

In summary, the 10In–Co–Ti sample exhibits the maximum catalytic response under photothermal excitation conditions. After this sample, the thermal, light alone, as well as the combined effect between energy sources, all decrease. A comparison with previous reports demonstrates the effectiveness of our systems.[39–41] For example, a relatively close non-noble-indium oxide catalyst ($Ni/C\text{-}In_2O_3$) exhibits a rate of 21 mmol g^{-1} h^{-1} at 352 °C under concentrated solar light.[42]

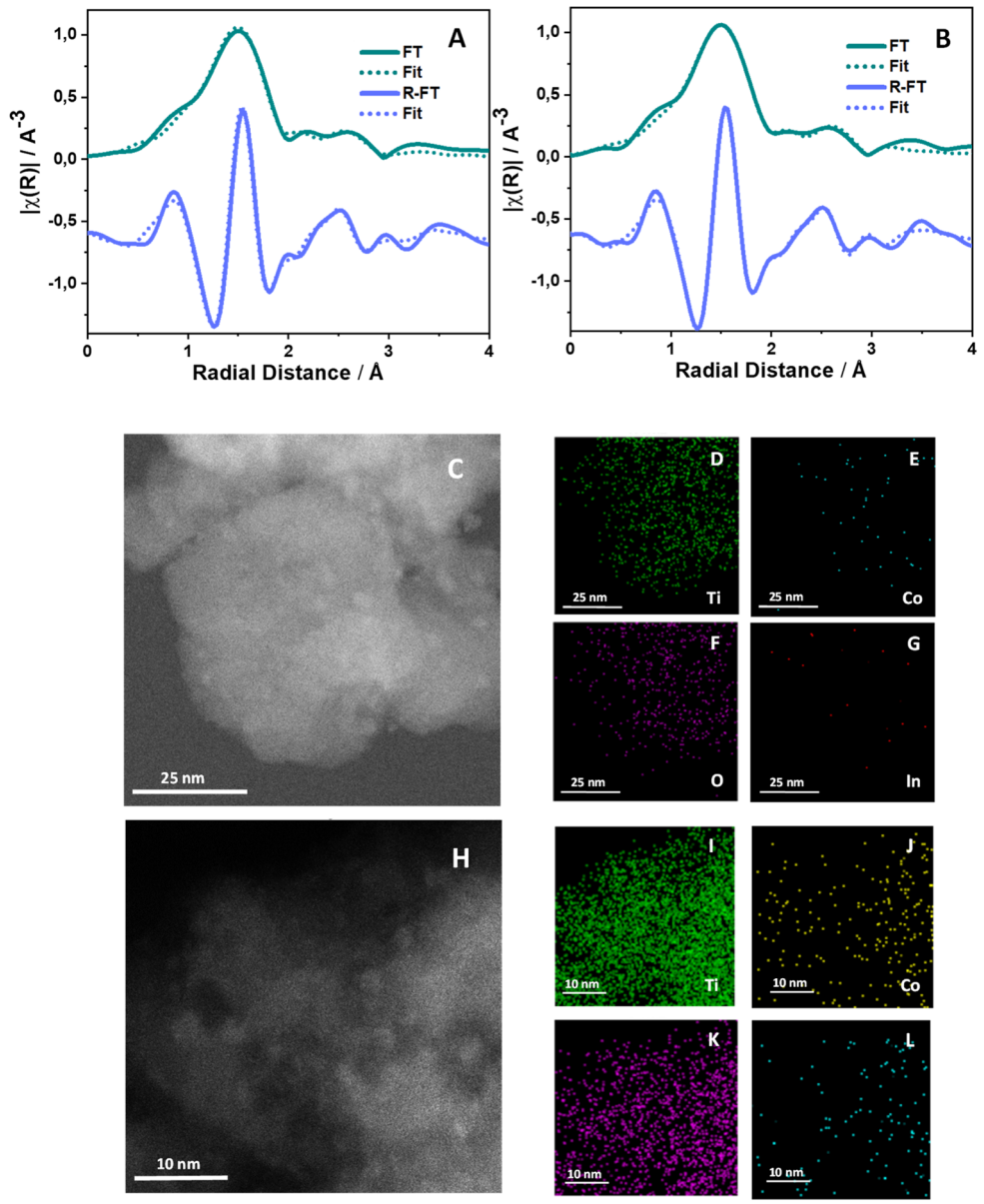

Fig. 6 (A) K^2-weighted real part (R-FT) and module (FT) of the Fourier transform of the Co K-edge EXAFS signal for the 2.5In–Co–Ti sample after a thermal reaction at 250 °C. (B) K^2-weighted real part (R-FT) and module (FT) of the Fourier transform of the Co K-edge EXAFS signal for the 2.5In–Co–Ti sample after a photothermal reaction at 250 °C. Experimental (R-FT and FT) and fitting results are presented. (C–G) Dark-field STEM (C) and EDS mapping for the 2.5In–Co–Ti sample after a thermal reaction at 250 °C. (H–L) Dark-field STEM (H) and EDS mapping for the 2.5In–Co–Ti sample after a photothermal reaction at 250 °C.

Although no exact comparison is possible due to the differences in reaction conditions, for the same temperature but with an illumination intensity two orders of magnitude inferior and classic thermal excitation, we obtained a rate of *ca.* 12 mmol g^{-1} h^{-1}. A final point to mention is the selectivity of the photothermal catalytic process. Rather high selectivity is obtained for all samples. As examples, 2.5In–Co–Ti shows a CO selectivity of 97.9%, and the 10In–Co–Ti catalysts achieve a selectivity of 98.5%. The exceptional selectivity is among the best reported to date (see ref. 43 and references therein).

3.4 Long-term stability and interpretation of synergy

To demonstrate the stability of the materials, a long-term stream test was conducted at 250 °C for 2.5In–Co–Ti and 10In–Co–Ti samples. The results are shown in Fig. 5F. It is noteworthy that activity under dark conditions is always lower than that under light conditions at the same temperature, and, as the graph shows, the responses to turning the light on and off are entirely reversible. In addition, no significant carbon deposition was observed from XPS (*i.e.*, the C/Ti ratio remains unchanged from the initial to the post-reaction samples), indicating the suitability of the ternary materials in order to use light to promote the (classical) thermal-related response of the studied solids.

Furthermore, the analysis of the 2.5In–Co–Ti sample was also carried out using Co K-edge EXAFS. The experimental signal and its fitting after the reaction under thermal conditions at a temperature of 250 °C are presented in Fig. 6A. The results obtained under photothermal conditions, at the same temperature, but under illumination, are visualized in Fig. 6B. No changes were observed in the fitting results obtained from samples subjected to different reaction conditions (Table 2). A similar result is obtained for the In K-edge, indicating that the Co and In species remain stable under both light and dark conditions at the same temperature. By performing the elemental analysis of the materials at a microscopic level using the EDS technique, it is observed that the Co and In species are well dispersed on the surface of anatase, both in the post-reaction samples at 250 °C under dark conditions (Fig. 6C–G) and at 250 °C under illuminated conditions (Fig. 6H–L). The comparison with the results presented in Fig. 2 further confirms the stability of the material. The same experiments were performed for the 10In–Co–Ti sample after the reaction. Fig. 7A shows the Co K-edge EXAFS fitting performed on the 10In–Co–Ti sample at 250 °C without light, and Fig. 7B shows the one obtained for the same sample at 250 °C under illumination. As in the case of the sample with a 2.5% indium content, there are no apparent differences between the two analyses. Also, as in the previous EDS images, good dispersion of the cobalt and indium components over the anatase component is observed in the samples under both conditions. The long-term catalytic stability would thus be grounded in the structural stability of the material under reaction conditions.

As suggested in the Introduction section, the thermal-alone behavior of the series can be directly linked to the different capabilities of CO_2 adsorption as a function of the indium content in the samples. To calibrate this issue, results for TPD experiments are presented in Fig. S5. A fitting of the TPD spectra was performed to estimate the fraction of CO_2 molecules present at the reaction temperature, which was roughly estimated by considering that molecules with desorption temperatures above *ca.* 300 °C do not contribute to the reaction. Such surface entities are adsorbed as carbonates (and others), poorly reactive and not easily involved in the reaction.[44] The amount of active CO_2 molecules, as measured considering the joint intensity of the two peaks observed at low temperature in Fig. S5, reaches a maximum with the 10In–Co–Ti sample. This fact would thus indicate that the thermal-alone behavior can be correlated with the effect of indium on the adsorption capabilities of the samples. Nevertheless, the analysis of the photoluminescence signal indicates that the cooperative effect achieved under dual excitation is not connected with the efficient use of photons at 250 °C. The photoluminescence intensity allows for the measurement of the charge carrier recombination, as the higher the intensity of the photoluminescence signal, the lower the recombination of charge carriers and, thus, the higher the chance of charge carriers participating in chemical reactions.[45] The behavior through the series of samples of the photoluminescence intensity (Fig. S6) and the excess function parameter (Fig. 5E) is not correlated, indicating that light and heat work cooperatively at the active center at a mechanistic level, likely modifying the coverage of specific intermediates and/or the interaction of such specific surface species with charge carriers. As stated, the total number of charge carriers reaching the surface does not play a critical role in controlling the synergy between light and heat.

An *in situ* infrared study was conducted to investigate the role of Co in the photothermal process (Fig. 8). To this end, the experiment was carried out with the sample and under the conditions (2.5In–Co–Ti sample; 250 °C) that maximize synergy between heat and light. As can be observed in the figure, relatively weak bands are developed in the case of the 2.5In–Ti reference powder as a function of time, irrespective of the (dark and illuminated) conditions, which is not the case for the 2.5In–Co–Ti sample. In this catalyst, the combined influence of temperature and illumination promotes the surface formation of formate species, as suggested by the appearance of the 1364 and 1565 cm^{-1} bands.[22,46] Therefore, the presence of cobalt appears to enhance the conversion of carbon dioxide into formate species ($CO_2 + H_2 \rightarrow HCOOH$), thereby facilitating its subsequent decarbonilation ($HCOOH \rightarrow CO + H_2O$). Thus, cobalt appears to promote the generation of CO and the water–gas shift reaction ($CO_2 + H_2 \leftrightarrow CO + H_2O$) through the carboxylate route.

In an attempt to rationalize the functional properties of the composite materials, Fig. 9 summarizes the functional and physicochemical properties of the solids. It presents the behavior through a series of samples that combine thermal and light properties, along with the structure of the samples that supports these functional properties. Note that the catalytic properties under photothermal conditions correspond to highly active and selective materials that are stable under long-term operation conditions. As detailed in Section 3.2, the local

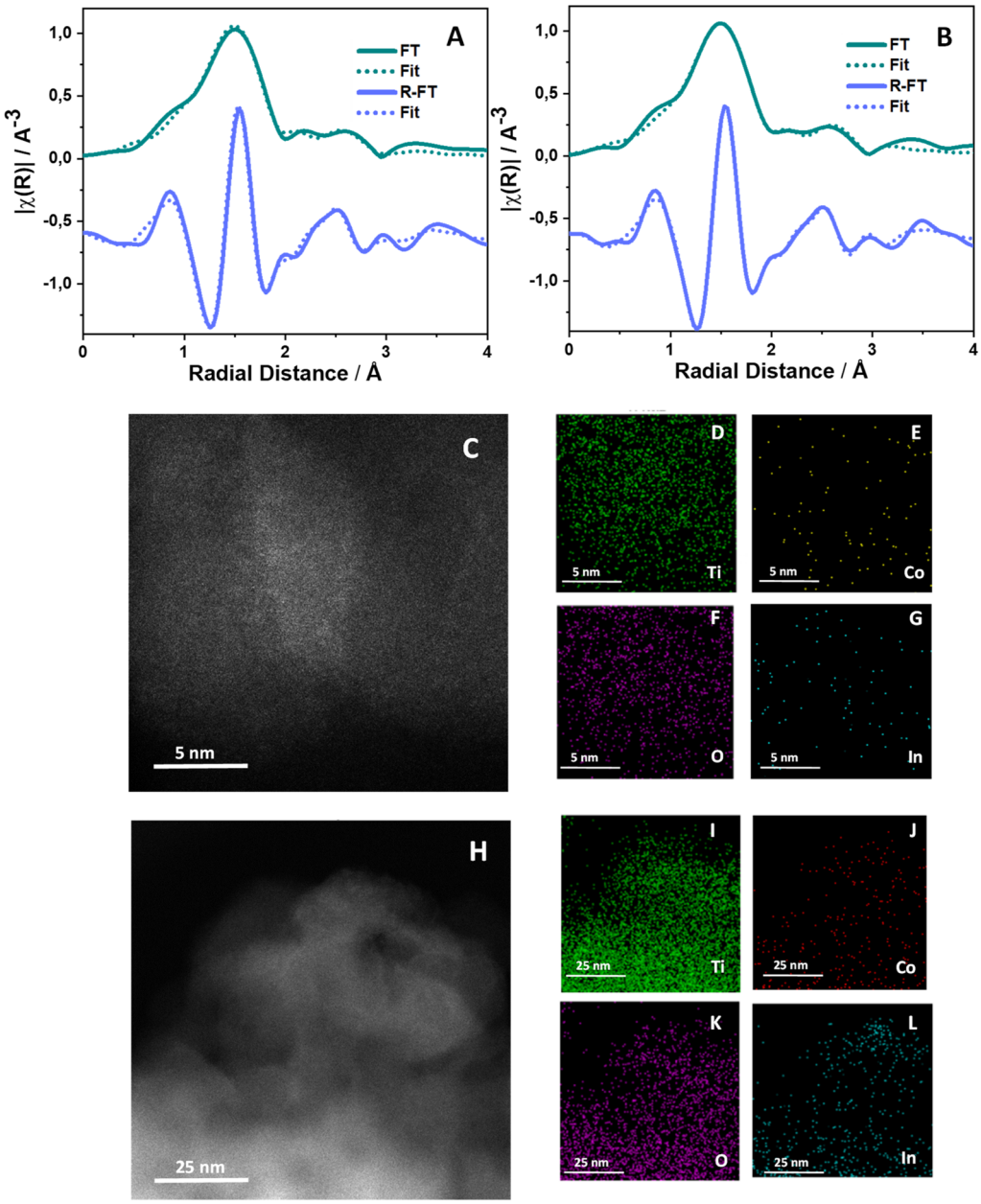

Fig. 7 (A) K^2-weighted real part (R-FT) and module (FT) of the Fourier transform of the Co K-edge EXAFS signal for the 10In–Co–Ti sample after a thermal reaction at 250 °C. (B) K^2-weighted real part (R-FT) and module (FT) of the Fourier transform of the Co K-edge EXAFS signal for the 10In–Co–Ti sample after a photothermal reaction at 250 °C. Experimental (R-FT and FT) and fitting results are presented. (C–G) Dark-field STEM (C) and EDS mapping for the 10In–Co–Ti sample after a thermal reaction at 250 °C. (H–L) Dark-field STEM (H) and EDS mapping for the 10In–Co–Ti sample after a photothermal reaction at 250 °C.

structures of cobalt and indium species can be classified into three different zones, as presented in Fig. 9, where structural properties can be visually linked to functional properties. The physico-chemical characterization pointed out the presence of sub-nanometric indium and cobalt entities for samples equal to or below the 10In–Co–Ti specimen. The presence of different cobalt entities is indicated by the two zones in blue. The combination of energy sources increases the catalytic response by *ca.* 2.9 times from the 2.5In–Co–Ti sample to the 10In–Co–Ti catalyst. The dual catalytic properties are thus enhanced in this region, and activity is maximized where sub-nanometric indium entities are detected, which occurs with relatively similar cobalt entities. However, for the optimum samples, the dominant presence of two-atom centers (Co–Co coordination number near 1) is observed. In contrast, samples with a lower indium content of 10% contain mainly isolated cobalt species (Fig. 4E and F). Although the interaction with titania is significant for both single and two-atom cobalt centers, the increase in the cobalt loading appears to modify such interaction (changes in Co–Ti coordination distances, Fig. 5F) and gradually favor the

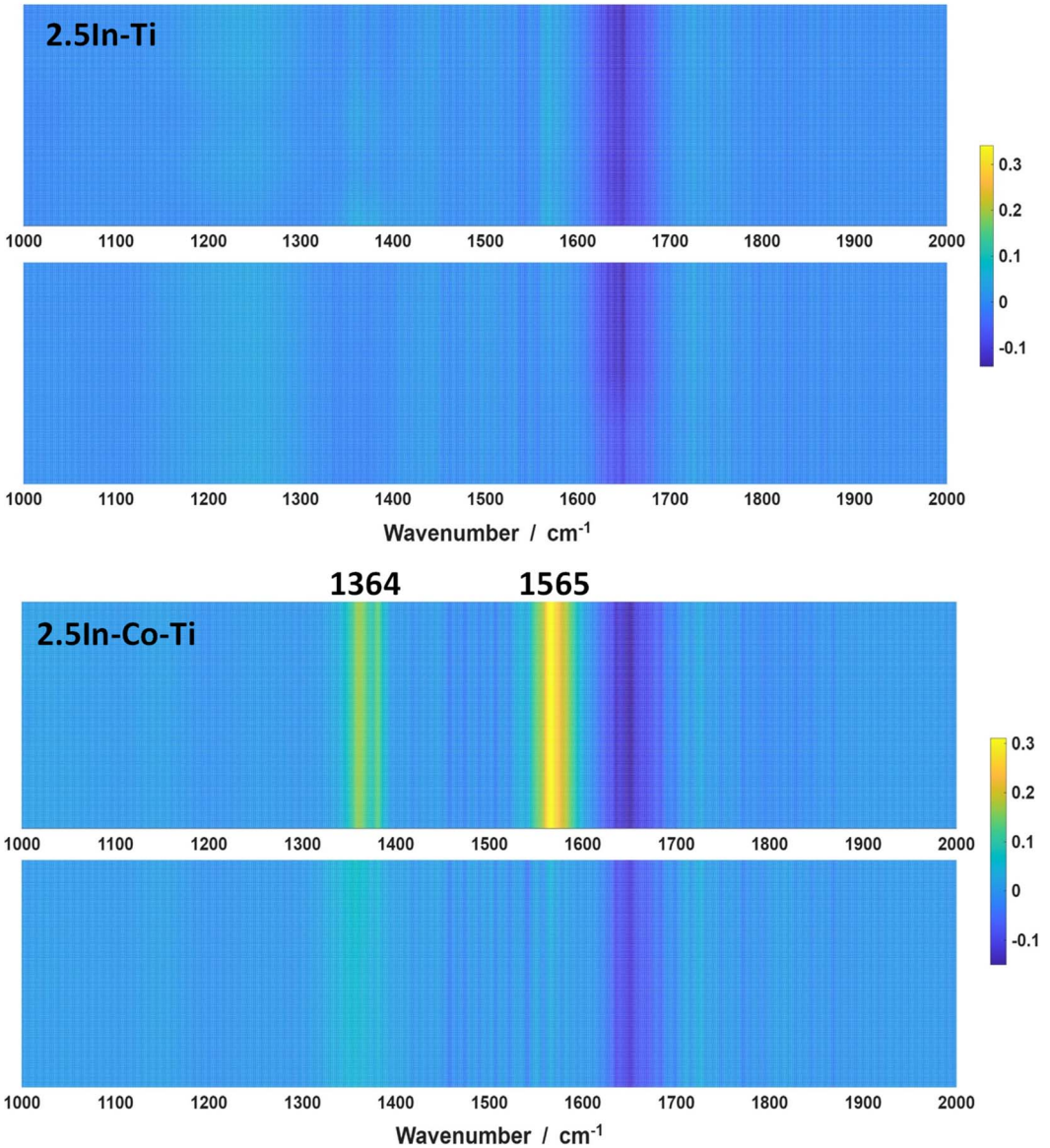

Fig. 8 *In situ* infrared results for the 2.5In–Co–Ti sample and 2.5In–Ti reference obtained under reaction conditions at 250 °C. For each material, the lower panel corresponds to results obtained under thermal excitation while the upper panel displays results under photothermal conditions.

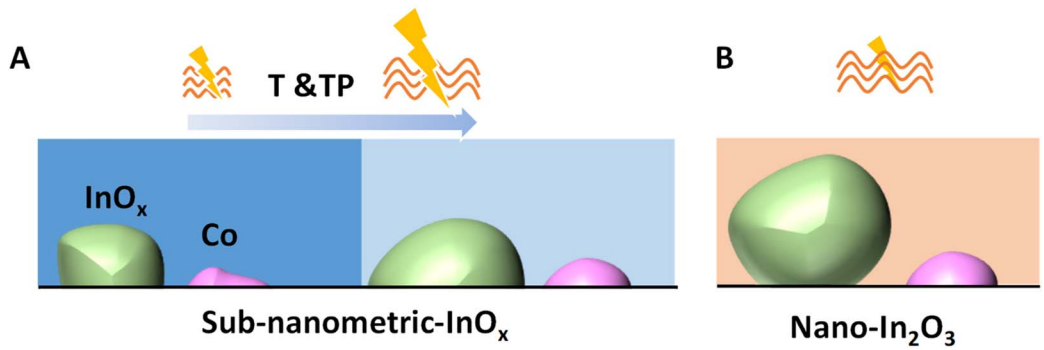

Fig. 9 Schematic representation of the photothermal effects and local structure of cobalt and indium species for (A) 2.5–15In–Co–Ti and (B) 20In–Co–Ti samples.

presence of Co–Co contacts. For samples with an indium content higher than 15%, the indium entities are in the nano-sized range. They exhibit an In K-edge EXAFS Fourier transform resembling that of the 6 nm pure indium oxide reference (Fig. S3). Their cobalt species are relatively similar to that observed for the 10In–Co–Ti sample. However, the dual-energy catalytic response and synergy are both decaying. As a result, the combination of subnanometric indium species with two-atom cobalt entities at the anatase surface maximizes activity and provides a strong combined effect between energy sources.

4 Conclusions

An important promotion of the photothermal valorization of CO_2 is achieved here using composite systems based on a dominant anatase component featuring sub-nanometric to nanometric indium and cobalt entities at its surface. To prove this, we synthesized materials using a single-pot microemulsion method, which ensures the maximum interaction and dispersion of the indium and cobalt entities at the surfaces of the main component (anatase). A series of catalysts with increasing indium content from 2.5 to 20 mol% was prepared, where the presence of cobalt-containing entities modulated the catalytic response of the oxide–oxide heterojunction. The resulting materials correspond to high surface area mesoporous composite materials.

The physicochemical characterization reveals that the indium species correspond to sub-nanometric species for samples with an indium content of up to approximately 15%. Above that point, nanometric-type structures of indium oxide are obtained. These indium-containing entities share the surface of the anatase with single-atom (samples having an indium content below 10%) or pairs of cobalt atoms at the anatase surface. Indium centers always exhibit an In(III) oxidation state, while the isolated cobalt atoms appear to have an intermediate Co(II)/Co(III) oxidation state, with the contribution of the Co(II) slightly increasing in the case of the cobalt pairs. The combination of subnanometric indium species with single cobalt atoms shows a modest thermal activity, but the dual excitation maximizes activity through the facile generation of formate species. A massive boost in thermal activity, likely related to the increase in the higher adsorption capability of CO_2 under reaction conditions (due to the increasing quantity of indium oxide-type entities in parallel to the indium content of the samples up to the 10% limit), is observed for samples up to the 10In–Co–Ti one. For this sample, the cooperative effect achieved under photothermal excitation is also important, providing the maximum activity. The 10In–Co–Ti sample is thus a highly active, stable, and highly selective material for the valorization of CO_2. Moreover, it also displays synergy between energy sources, opening a pathway for intensifying the corresponding classical thermal process.

Author contributions

R. S.-C: conceptualization; investigation; visualization; writing – original draft. E. F.-G: investigation; visualization. I. B.-N: investigation; visualization; writing – review & editing. U. C.-F: investigation; funding acquisition; project administration; resources; validation; visualization; writing – review & editing. L. M.: investigation. J. A. R.: investigation; funding acquisition; project administration; writing – review & editing. M. F.-G.: conceptualization; investigation; funding acquisition; project administration; software; supervision; writing – original draft; writing – review & editing. A. K.: conceptualization; investigation; funding acquisition; project administration; software; supervision; writing – original draft; writing – review & editing.

Conflicts of interest

The authors declare no competing interest.

Data availability

Data will be made available on request.

Supplementary information: contains information about the reactor configuration, catalytic parameters and properties, EXAFS, TPD, and optoelectronic characterization data. See DOI: https://doi.org/10.1039/d5ta07547e.

Acknowledgements

The authors acknowledge the financial support through the project IN116424 and IV100124 PAPIIT-UNAM, Mexico and through grant PID2022-136883OB-C21 by MCIU/AEI/10.13039/501100011033 and by the "European Union" FEDER/EU programs. The authors thank D. A. Dominguez, P. Casillas, C. Gonzalez and J. Romero for the technical support provided. M. F. G. is fully indebted to Prof. F. Fernández-Martín for general discussions. I. B.-N. thanks Brookhaven National Laboratory for funding through the Goldhaber Distinguished Fellowship Program. The XAS studies were performed at the 8-ID and 7-ID beamlines of the National Synchrotron Light Source II, a U.S. Department of Energy (DOE) Office of Science User Facility operated for the DOE Office of Science by Brookhaven National Laboratory under Contract No. DE-SC0012704.

References

1 A. Álvarez, A. Bansode, A. Urakawa, A. V. Bavykina, T. A. Wezendonk, M. Makkee, J. Gascon and F. Kapteijn, *Chem. Rev.*, 2017, **117**, 9804–9838.
2 Q. Lu, J. Rosen, Y. Zhou, G. S. Hutchings, Y. C. Kimmel, J. G. Chen and F. Jiao, *Nat. Commun.*, 2014, **5**, 3242.
3 X. Li, J. Yu, M. Jaroniec and X. Chen, *Chem. Rev.*, 2019, **119**, 3962–4179.
4 F. Zhang, Y.-H. Li, M.-Y. Qi, Y. M. A. Yamada, M. Anpo, Z.-R. Tang and Y.-J. Xu, *Chem Catal.*, 2021, **1**, 272–297.
5 C. Hu, S. Tu, N. Tian, T. Ma, Y. Zhang and H. Huang, *Angew. Chem., Int. Ed.*, 2021, **60**, 16309–16328.
6 S. Fang and Y. H. Hu, *Chem. Soc. Rev.*, 2022, **51**, 3609–3647.
7 M. Ghoussoub, M. Xia, P. N. Duchesne, D. Segal and G. Ozin, *Energy Environ. Sci.*, 2019, **12**, 1122–1142.

8 V. Nair, M. J. Muñoz-Batista, M. Fernández-García, R. Luque and J. C. Colmenares, *ChemSusChem*, 2019, **12**, 2098–2116.
9 J. Zhou, H. Liu and H. Wang, *Chin. Chem. Lett.*, 2023, **34**, 107420.
10 M. I. Alam, R. Cheula, G. Moroni, L. Nardi and M. Maestri, *Catal. Sci. Technol.*, 2021, **11**, 6601–6629.
11 J. H. A. Schuurmans, T. M. Masson, S. D. A. Zondag, P. Buskens and T. Noël, *ChemSusChem*, 2024, **17**, e202301405.
12 F. Fresno, A. Iglesias-Juez and J. M. Coronado, *Top. Curr. Chem.*, 2023, **381**, 21.
13 Y. Chen, Y. Ding, W. Han, W. Li, X. Yu and G. Tian, *J. Mater. Chem. A*, 2023, **11**, 8342–8351.
14 I. Barba-Nieto, N. Gómez-Cerezo, A. Kubacka and M. Fernández-García, *Catal. Sci. Technol.*, 2021, **11**, 6904–6930.
15 Z. Sun, X. Huang and G. Zhang, *J. Cleaner Prod.*, 2022, **381**, 135156.
16 L. Wang, Y. Dong, T. Yan, Z. Hu, A. A. Jelle, D. M. Meira, P. N. Duchesne, J. Y. Y. Loh, C. Qiu, E. E. Storey, Y. Xu, W. Sun, M. Ghoussoub, N. P. Kherani, A. S. Helmy and G. A. Ozin, *Nat. Commun.*, 2020, **11**, 2432.
17 Z. Wang, Z. Yang, Z. C. Kadirova, M. Guo, R. Fang, J. He, Y. Yan and J. Ran, *Coord. Chem. Rev.*, 2022, **473**, 214794.
18 R. Sayago-Carro, I. Barba-Nieto, U. Caudillo-Flores, Á. Tolosana-Moranchel, J. A. Rodríguez, M. Fernández-García and A. Kubacka, *ACS Appl. Mater. Interfaces*, 2024, **16**, 33461–33474.
19 D. Leshchev, M. Rakitin, B. Luvizotto, R. Kadyrov, B. Ravel, K. Attenkofer and E. Stavitski, *J. Synchrotron Radiat.*, 2022, **29**, 1095–1106.
20 A. Kubacka, U. Caudillo-Flores, I. Barba-Nieto, M. J. Muñoz-Batista and M. Fernández-García, *Curr. Opin. Colloid Interface Sci.*, 2020, **49**, 42–59.
21 R. Fiorenza, M. Bellardita, S. A. Balsamo, L. Spitaleri, A. Gulino, M. Condorelli, L. D'Urso, S. Scirè and L. Palmisano, *Chem. Eng. J.*, 2022, **428**, 131249.
22 R. Sayago-Carro, M. N. Gómez-Cerezo, M. Fernández-García and A. Kubacka, *J. Cleaner Prod.*, 2023, **429**, 139542.
23 R. Sayago-Carro, I. Barba-Nieto, N. Gómez-Cerezo, J. A. Rodriguez, M. Fernández-García and A. Kubacka, *ACS Appl. Mater. Interfaces*, 2024, **16**, 62131–62141.
24 M. Thommes, K. Kaneko, A. V. Neimark, J. P. Olivier, F. Rodriguez-Reinoso, J. Rouquerol and K. S. W. Sing, *Pure Appl. Chem.*, 2015, **87**, 1051–1069.
25 M. Fernández-García, A. Martínez-Arias, J. C. Hanson and J. A. Rodriguez, *Chem. Rev.*, 2004, **104**, 4063–4104.
26 J. Ederth, P. Johnsson, G. A. Niklasson, A. Hoel, A. Hultåker, P. Heszler, C. G. Granqvist, A. R. van Doorn, M. J. Jongerius and D. Burgard, *Phys. Rev. B: Condens. Matter Mater. Phys.*, 2003, **68**, 155410.
27 H. Yan, X. Wang, M. Yao and X. Yao, *Prog. Nat. Sci.:Mater. Int.*, 2013, **23**, 402–407.
28 G. Jagannath, B. Eraiah, A. Gaddam, H. Fernandes, D. Brazete, K. Jayanthi, K. N. Krishnakanth, S. Venugopal Rao, J. M. F. Ferreira, K. Annapurna and A. R. Allu, *J. Phys. Chem. C*, 2019, **123**, 5591–5602.
29 P. E. Moulder, J. F. Stickle and W. F. Sobol, *Handbook of X-Ray Photoelectron Spectroscopy: A Reference Book of Standard Data for Use in X-ray Photoelectron Spectroscopy*, Perkin-Elmer, 1993.
30 Z.-P. Hu, G. Qin, J. Han, W. Zhang, N. Wang, Y. Zheng, Q. Jiang, T. Ji, Z.-Y. Yuan, J. Xiao, Y. Wei and Z. Liu, *J. Am. Chem. Soc.*, 2022, **144**, 12127–12137.
31 H. Dau, P. Liebisch and M. Haumann, *Anal. Bioanal. Chem.*, 2003, **376**, 562–583.
32 F. Mikaeili, M. M. Rahaman and P. Gouma, *Adv. Sci.*, 2025, **12**, 2502981.
33 J. D. Henderson, L. Pearson, H. Nie and M. C. Biesinger, *Surf. Interface Anal.*, 2025, **57**, 81–97.
34 *X-Ray Absorption and X-Ray Emission Spectroscopy*, ed. J. A. Van Bokhoven and C. Lamberti, Wiley, 2016.
35 P. A. Lee, P. H. Citrin, P. Eisenberger and B. M. Kincaid, *Rev. Mod. Phys.*, 1981, **53**, 769–806.
36 X-Ray Absorption Techniques and Related Techniques, *International Tables for Crystallography*, ed. C. T. Chantler, F. Boscherini and B. Bunker, International Union of Crystallography, Chester, England, 2020, vol. I.
37 R. D. Shannon, *Acta Crystallogr., Sect. A*, 1976, **32**, 751–767.
38 S. E. Braslavsky, A. M. Braun, A. E. Cassano, A. V Emeline, M. I. Litter, L. Palmisano, V. N. Parmon and N. Serpone, *Pure Appl. Chem.*, 2011, **83**, 931–1014.
39 Z. Jing, Q. Wang, C.-M. Fan, X.-F. Yang, P.-Y. Tang and B. Li, *J. Mater. Chem. A*, 2025, **13**, 18253–18282.
40 X. Guo, F. Zhang, Y. Zhang and J. Hu, *J. Mater. Chem. A*, 2023, **11**, 7331–7343.
41 A. Mena-Saucedo, U. Caudillo-Flores, A. Kubacka and M. Fernández-García, *J. Phys. Chem. C*, 2024, **128**, 20923–20932.
42 S. Mo, S. Li, J. Zhou, X. Zhao, H. Zhao, X. Zhou, Y. Fan, Z. Zhu, B. Li, Q. Xie, W. Si, Y. Chen, D. Ye and J. Li, *ACS Catal.*, 2025, **15**, 2796–2808.
43 D. Chu, M. Xu, Y. Zou, C. Xing, D. Sun and L. Ling, *ACS Catal.*, 2025, **15**, 11266–11276.
44 A. Wesner, P. Kampe, N. Herrmann, S. Eller, C. Ruhmlieb and J. Albert, *ChemCatChem*, 2023, **15**, e202301125.
45 J. Liqiang, Q. Yichun, W. Baiqi, L. Shudan, J. Baojiang, Y. Libin, F. Wei, F. Honggang and S. Jiazhong, *Sol. Energy Mater. Sol. Cells*, 2006, **90**, 1773–1787.
46 B. Deng, H. Song, K. Peng, Q. Li and J. Ye, *Appl. Catal., B*, 2021, **298**, 120519.